EINDHOVEN UNIVERSITY OF TECHNOLOGY

Micromechanical modeling of anisotropic behavior of oriented semicrystalline polymers

Citation for published version (APA):
Mirkhalaf, M., van Dommelen, H., Govaert, L., Furmanski, J., & Geers, M. (2019). Micromechanical modeling of anisotropic behavior of oriented semicrystalline polymers. *Journal of Polymer Science, Part B: Polymer Physics*, *57*(7), 378-391. https://doi.org/10.1002/polb.24791

DOI:
10.1002/polb.24791

Document status and date:
Published: 01/04/2019

Document Version:
Accepted manuscript including changes made at the peer-review stage

Please check the document version of this publication:

• A submitted manuscript is the version of the article upon submission and before peer-review. There can be important differences between the submitted version and the official published version of record. People interested in the research are advised to contact the author for the final version of the publication, or visit the DOI to the publisher's website.
• The final author version and the galley proof are versions of the publication after peer review.
• The final published version features the final layout of the paper including the volume, issue and page numbers.

Link to publication

General rights
Copyright and moral rights for the publications made accessible in the public portal are retained by the authors and/or other copyright owners and it is a condition of accessing publications that users recognise and abide by the legal requirements associated with these rights.

• Users may download and print one copy of any publication from the public portal for the purpose of private study or research.
• You may not further distribute the material or use it for any profit-making activity or commercial gain
• You may freely distribute the URL identifying the publication in the public portal.

If the publication is distributed under the terms of Article 25fa of the Dutch Copyright Act, indicated by the “Taverne” license above, please follow below link for the End User Agreement:

www.tue.nl/taverne

Take down policy
If you believe that this document breaches copyright please contact us at:

openaccess@tue.nl

providing details and we will investigate your claim.

Download date: 04. Oct. 2023

Micro-mechanical modelling of anisotropic behaviour of oriented semi-crystalline polymers

S.M. Mirkhalaf,[1] J.A.W. van Dommelen,[1] L.E. Govaert,[1] J. Furmanski,[2] M.G.D. Geers[1]

[1]Department of Mechanical Engineering, Eindhoven University of Technology, P.O. Box 513, 5600 MB Eindhoven, The Netherlands.

[2]ExxonMobil Research and Engineering, Annandale, NJ, 08801, United States

Corresponding to: J.A.W. van Dommelen(J.A.W.v.Dommelen@tue.nl)

Dated: January 24, 2019

ABSTRACT: Some manufacturing processes of polymeric materials, such as injection moulding or film blowing, cause the final product to be highly anisotropic. In this study, the mechanical behaviour of drawn Polyethylene (PE) tapes is investigated via micro-mechanical modelling. An elasto-viscoplastic micro-mechanical model, developed within the framework of the so-called composite inclusion model, is presented to capture the anisotropic behaviour of oriented semi-crystalline Polyethylene. Two different phases namely, amorphous and crystalline (both described by elasto-viscoplastic constitutive models), are considered at the micro-structural level. The initial oriented crystallographic structure of the drawn tapes is taken into account. It was previously shown[1] that by only considering the oriented crystallographic structure, it is not possible to capture the macroscopic anisotropic behaviour of drawn tapes. The main contribution of this study is the development of an anisotropic model for the amorphous phase within the micro-mechanical framework. An EGP (Eindhoven Glassy Polymer) based model including different sources of anisotropy namely, anisotropic elasticity, internal stress in the elastic network and anisotropic viscoplasticity, is developed for the amorphous phase and incorporated into the micro-mechanical model. Comparisons against experimental results reveal remarkable improvements of the model predictions (compared to micro-mechanical model predictions including isotropic amorphous domains) and thus the significance of the amorphous phase anisotropy on the overall behavior of drawn PE tapes.

Keywords: Semi-crystalline Polymers, Oriented Polyethylene, Micro-mechanical model, Anisotropic amorphous phase

INTRODUCTION

Polymers have become an important and highly applicable type of materials due to their interesting chemical, optical, thermal and mechanical properties. Some polymeric materials develop a semi-crystalline micro-structure during the cooling process from the molten state. The micro-structure of semi-crystalline polymers is composed of different phases, a crystalline phase and an amorphous phase[2].

During some manufacturing processes for polymeric products, such as injection molding or film blowing, the material is under shear and elongational flow resulting in an oriented micro-structure after crystallization which leads to anisotropic mechanical behaviour. Semi-crystalline polymers are used in different industries and in load bearing applications. Load and lifetime assessments require to predict the orientation dependent thermo-mechanical behaviour of these materials in a quantitative manner, based on the inherently hierarchical heterogeneous structure of semi-crystalline polymers, using multi-scale simulations.

The history of micro-mechanical modelling of semi-crystalline polymers dates back to the 1990's. Parks and Ahzi[3] and Lee et al.[4,5] were the pioneers in modelling the mechanical behaviour of semi-crystalline polymers within a micro-mechanical framework. Parks and Ahzi[3] developed a fully crystalline micro-mechanical rigid-viscoplastic model (named Constrained Hybrid (CH) model) to describe the deformation behaviour and texture evolution of polycrystalline materials. Ahzi et al.[7] described large plastic deformation and also texture evolution of different semi-crystalline polymers with the CH model proposed by Parks and Ahzi[3] and the reformulated version of the CH model by Lee et al.[6], in which idealized fully crystalline materials were considered and the deformation mechanism was assumed to be crystallographic slip only. A rigid viscoplastic so-called *composite inclusion model* was developed by Lee et al.[4,5] to describe the large plastic deformation of semi-crystalline polymers as well as the texture evolution in the crystalline phases by taking into account both crystalline and amorphous phases. The model by Lee et al.[4,5] was extended by van Dommelen et al.[2] to include elasticity and as a result, the original rigid-viscoplastic model was reformulated to an elasto-viscoplastic model. Nikolov and Doghri[8] developed a micro-mechanical model to describe the small deformation behaviour of Polyethylene. The material was considered

as a composite consisting of a number of rigid viscoplastic crystalline lamellae together with their adjacent amorphous layers which were described as a viscoelastic material. Nikolov et al.[9] extended this model[8], where the crystalline phase was modelled by an elasto-viscoplastic model and the amorphous phase was described using a new physically derived viscoelastic model. Adequate agreements were obtained between simulations and experimentally obtained tensile stress-strain curves at small deformations.

Sedighiamiri et al.[10] modified the model developed by van Dommelen et al.[2] by extending the slip kinetics for semi-crystalline PE. The relation between the shear rate of each slip system and the corresponding resolved shear stress was described with an Eyring flow rule. Also, the flow rule of the amorphous phase was based on an Eyring model. Sedighiamiri et al.[11] added a non-Schmid effect to the constitutive relation for each slip system, to predict the yield kinetics in different deformation modes and failure of semi-crystalline PE. The yield kinetics of initially isotropic PE was well described with this model. Sedighiamiri et al.[1] also investigated the possibility of using the previously developed models[10,11] for initially oriented semi-crystalline PE. In addition, it was studied whether oriented systems could be used for characterizing the properties of different crystallographic slip systems. Based on wide angle X-ray scattering measurements, the initial orientation distribution was obtained. Uniaxial tensile tests were performed on dog-bone-shaped samples which were cut from a tape at different angles to investigate the orientation effects. It was concluded that for more accurate quantitative predictions, it is required to describe the amorphous phase using an anisotropic model which takes into account the amorphous phase orientation.

The goal of this study is to model the mechanical behaviour of hot drawn PE tapes. Not only are these tapes highly anisotropic with a significant effect of the loading angle on the overall deformation behaviour, also a large strain rate dependency exists, specifically when the sample is cut in the draw direction of the tape. The model, presented in this study, therefore extends the model developed by Sedighiamiri et al.[10,11], which was used for isotropic high density Polyethylene (HDPE) and oriented PE tapes possessing a highly oriented crystallographic structure[1]. In this work, an anisotropic model, including different sources of anisotropy, namely anisotropic elasticity, an internal stress in the elastic network and anisotropic viscoplastic flow, is developed and incorporated into the micro-mechanical

model. Poluektov et al.[15] extended previous work[16,17] to quantitatively study the long term and short term mechanical behaviour of anisotropic PET. For that purpose, an internal stress was incorporated into the constitutive description of the amorphous phase. The same approach is followed in this study. However, the anisotropic model developed in this study has an additional anisotropic viscoplastic flow rule which is developed using the anisotropic effective stress of Hill[18,19]. The effect of the amorphous phase anisotropy is significant and comparisons between the model predictions and experimentally obtained results show significant improvements.

The next section gives the experimental results for oriented PE tape under different loading angles and different strain rates, reported by Sedighiamiri et al.[1]. In Section , the micromechanical framework, including the original *isotropic* model for the amorphous phase, is explained. Based on the results with this model and comparisons to experimental results, the motivation for extending the constitutive model for the amorphous phase is discussed. Section explains various sources of anisotropy in oriented PE tapes and describes the *anisotropic* model for the amorphous phase, including an internal stress into the elastic network, an anisotropic viscoplastic flow rule and anisotropic elasticity. In Section , the material properties for the individual micro-structural phases are given and the Hill parameters and pre-stretch factor for the amorphous phase are quantified. Comparisons between the simulations and experimental results are made. Section summarizes the conclusions drawn from this study.

EXPERIMENTAL RESULTS

In this study, the mechanical anisotropy of hot-drawn Polyethylene tapes, in which the crystalline domains show a preferred orientation distribution is modelled. Sedighiamiri et al.[1] conducted tensile experiments on oriented high density Polyethylene tape with a draw ratio of 4 ($\lambda = 4$) at different loading angles ($\phi = 0°, 20°, 50°$) and under different strain rates. Wide angle X-ray scattering (WAXS) experiments were conducted and the weight fraction of the crystalline phase of the oriented Polyethylene tape was determined to be 66%. Additional WAXS experiments were conducted to obtain the crystallographic orientation distribution.

Uniaxial tensile tests were performed on dog-bone-shaped samples which were cut from the tapes at different angles to investigate the orientation effects. Three different strain rates, within the quasi-static range, were applied ($\dot{\varepsilon} = 0.0001\ \mathrm{s}^{-1}, 0.001\ \mathrm{s}^{-1}, 0.01\ \mathrm{s}^{-1}$). Figure 1 shows a schematic representation of the samples cut from the oriented tapes at different angles with respect to the machine direction, together with the experimentally obtained stress-strain curves at room temperature.

Figure 1.

A strong degree of dependence on both loading angle and strain rate is observed in the stress-strain curves.

MICRO-MECHANICAL MODEL

In this section, the micro-mechanical model, used in this study, including the original *isotropic* model for the amorphous phase, is presented[11]. The model has four key components which constitute the basis of the model:

- Two-phase composite inclusion;
- Inclusion interaction law;
- Constitutive model of the crystalline phase;
- Constitutive model of the amorphous phase.

Each of the aforementioned aspects of the micro-mechanical model will be explained in detail in the following.

Two-phase composite inclusion

Lee et al.[4,5] proposed a framework for modelling the rigid/viscoplastic mechanical behaviour of semi-crystalline materials. This framework uses a layered two-phase composite inclusion as the basis of the model, whereby an aggregate of inclusions constitutes the whole material. This approach is used in this study. Each crystalline lamella and the corresponding attached amorphous layer, as shown in Figure 2(a), is considered as an inclusion.

Figure 2.

The volume-averaging relations for the deformation gradient tensor and Cauchy stress tensor apply:

$$\mathbf{F}^I = f_0^a \mathbf{F}^a + (1 - f_0^a)\mathbf{F}^c, \tag{1}$$

$$\boldsymbol{\sigma}^I = f^a \boldsymbol{\sigma}^a + (1 - f^a)\boldsymbol{\sigma}^c, \tag{2}$$

where $\mathbf{F}^I$ is the inclusion-averaged deformation gradient, $\boldsymbol{\sigma}^I$ is the inclusion-averaged Cauchy stress, f_0^a and f^a are the initial and current volume fraction of the amorphous phase, respectively. The following relation holds for the current volume fraction of each constituent phase[2]:

$$f^\pi = \frac{f_0^\pi J^\pi}{f_0^a J^a + (1 - f_0^a) J^c}; \qquad \pi = a, c, \tag{3}$$

where J represents the corresponding volume change ratio ($\det(\mathbf{F})$). The superscripts a, c and I refer to the amorphous phase, the crystalline phase and the inclusion, respectively. Compatibility of deformation gradients and traction equilibrium are considered at the interface between the constituents. If $\mathbf{n}^I$ is the unit normal vector on the interface in the deformed configuration, traction equilibrium is obtained by:

$$\boldsymbol{\sigma}^a \cdot \mathbf{n}^I = \boldsymbol{\sigma}^c \cdot \mathbf{n}^I = \boldsymbol{\sigma}^I \cdot \mathbf{n}^I, \tag{4}$$

The compatibility condition is obtained by:

$$\mathbf{F}^a \cdot \mathbf{x}_0^I = \mathbf{F}^c \cdot \mathbf{x}_0^I = \mathbf{F}^I \cdot \mathbf{x}_0^I, \tag{5}$$

where, $\mathbf{x}_0^I$ denotes an arbitrary vector in the interface plane in the reference configuration.

Inclusion interaction law

The semi-crystalline polymer is considered as an aggregate of randomly or preferentially oriented inclusions for isotropic and anisotropic materials, respectively. Figure 2(b) depicts a schematic representation of an aggregate of uniformly distributed inclusions. A local-global interaction law is defined to relate the mechanical behaviour of each composite inclusion to the imposed boundary conditions of the aggregate of inclusions. In this work, a hybrid interaction model, which is basically an intermediate approach between the Taylor and Sachs

interaction laws and referred to as the $\hat{\mathbf{U}}$-inclusion model, is used[2]. In the hybrid interaction law, six auxiliary deformation-like unknowns, $\hat{\mathbf{U}}$, are introduced for which the following local-global relation holds:

$$\mathbf{U}^{I^i} \cdot \mathbf{n}_0^{I^i} = \hat{\mathbf{U}} \cdot \mathbf{n}_0^{I^i}, \qquad i = 1, \ldots, N^I \tag{6}$$

where N^I is the number of inclusions and $\mathbf{U}$ is the right stretch tensor, such that $\mathbf{F} = \mathbf{R} \cdot \mathbf{U}$, where $\mathbf{R}$ is the rotation tensor. Using the global (macroscopic) Cauchy stress tensor $\overline{\boldsymbol{\sigma}}$, and the global rotation tensor, $\overline{\mathbf{R}}$, the following local-global relations hold:

$$\boldsymbol{\sigma}^{I^i} \cdot \mathbf{x}^{I^i} = \overline{\boldsymbol{\sigma}} \cdot \mathbf{x}^{I^i}, \qquad i = 1, \ldots, N^I, \tag{7}$$

$$\mathbf{R}^{I^i} = \overline{\mathbf{R}}, \qquad i = 1, \ldots, N^I, \tag{8}$$

in combination with the following consistency conditions:

$$\overline{\boldsymbol{\sigma}} = \sum_{i=1}^{N^I} f^{I^i} \boldsymbol{\sigma}^{I^i}, \tag{9}$$

$$\overline{\mathbf{U}} = \left(\frac{\overline{J}}{J_{\sum}} \right)^{1/3} \sum_{i=1}^{N^I} f_0^{I^i} \mathbf{U}^{I^i}, \tag{10}$$

where, $\overline{J}$ and $J_{\sum}$ are given by:

$$\overline{J} = \sum_{i=1}^{N^I} f_0^{I^i} J^{I^i}, \tag{11}$$

$$J_{\sum} = \det \left(\sum_{i=1}^{N^I} f_0^{I^i} \mathbf{F}^{I^i} \right). \tag{12}$$

In relation (7), $\mathbf{x}^{I^i}$ denotes an arbitrary vector in the interface plane of each composite inclusion.

Before detailing the constitutive relations for the crystalline and amorphous phases, it is necessary to mention that for the both phases, the deformation gradient is assumed to be multiplicatively decomposed into its elastic and plastic components, depicted by subscripts e and p, respectively[23]:

$$\mathbf{F} = \mathbf{F}_e \cdot \mathbf{F}_p. \tag{13}$$

This decomposition suggests a local unstressed intermediate configuration obtained by elastic unloading from the final deformed configuration. The velocity gradient is given by:

$$\mathbf{L} = \mathbf{L}_e + \mathbf{F}_e \cdot \mathbf{L}_p \cdot {\mathbf{F}_e}^{-1}, \tag{14}$$

where the elastic velocity gradient, $\mathbf{L}_e$, and plastic velocity gradient, $\mathbf{L}_p$, are defined by:

$$\mathbf{L}_e = \dot{\mathbf{F}}_e \cdot {\mathbf{F}_e}^{-1}, \tag{15}$$

$$\mathbf{L}_p = \dot{\mathbf{F}}_p \cdot {\mathbf{F}_p}^{-1}. \tag{16}$$

Crystalline phase constitutive model

The crystalline domain of HDPE has an orthorhombic structure with anisotropic properties, including a high elastic modulus in the chain direction. The elastic stress-strain relation for the crystalline phase is given by:

$$\mathbf{S}^c = {}^4\mathsf{C}^c : \mathbf{E}_e^c, \tag{17}$$

where the elastic second Piola-Kirchhoff stress, $\mathbf{S}^c$, is defined by:

$$\mathbf{S}^c = J_e^c \mathbf{F}_e^{c-1} \cdot \boldsymbol{\sigma}^c \cdot \mathbf{F}_e^{c-T}, \tag{18}$$

where $\mathbf{F}_e^c$ denotes the elastic deformation gradient tensor in the crystalline phase and $\boldsymbol{\sigma}^c$ is the Cauchy stress tensor. In Equation (17), the elastic Green-Lagrange strain, $\mathbf{E}_e^c$, is defined by:

$$\mathbf{E}_e^c = \frac{1}{2}\left(\mathbf{F}_e^{cT} \cdot \mathbf{F}_e^c - \mathbf{I}\right), \tag{19}$$

where $\mathbf{I}$ is the second order identity tensor. In Equation (17), ${}^4\mathsf{C}^c$ denotes the elasticity tensor which, in matrix form using the Voigt notation (where the stress components are ordered as $\underset{\sim}{\sigma}^T = [\sigma_{11} \;\; \sigma_{22} \;\; \sigma_{33} \;\; \sigma_{12} \;\; \sigma_{13} \;\; \sigma_{23}]$), can be represented by:

$$\underline{\mathsf{C}} = \begin{bmatrix} c_{11} & c_{12} & c_{13} & 0 & 0 & 0 \\ c_{12} & c_{22} & c_{23} & 0 & 0 & 0 \\ c_{13} & c_{23} & c_{33} & 0 & 0 & 0 \\ 0 & 0 & 0 & c_{44} & 0 & 0 \\ 0 & 0 & 0 & 0 & c_{55} & 0 \\ 0 & 0 & 0 & 0 & 0 & c_{66} \end{bmatrix}. \tag{20}$$

The plastic behaviour of the crystalline phase is assumed to occur by crystallographic slip up to moderate strains[25–28]. In the micro-mechanical model, the slip mode is considered to be merely fine slip. A rate dependent crystal plasticity model is used to describe the viscoplastic part of the deformation in the crystalline lamellae. The contribution of all physically distinct slip systems is taken into account:

$$\mathbf{L}_p^c = \dot{\mathbf{F}}_p^c \cdot \mathbf{F}_p^{c\,-1} = \sum_{\alpha=1}^{N_s} \dot{\gamma}^\alpha \mathbf{P}_0^\alpha, \tag{21}$$

where N_s is the number of physically distinct slip systems, $\mathbf{P}_0^\alpha$ is the nonsymmetric Schmid tensor given by:

$$\mathbf{P}_0^\alpha = \mathbf{s}_0^\alpha \otimes \mathbf{n}_0^\alpha, \tag{22}$$

where, $\mathbf{s}_0^\alpha$ is the unit slip direction and $\mathbf{n}_0^\alpha$ is the unit slip plane normal of slip system α, both in the reference configuration. In Equation (21), $\dot{\gamma}^\alpha$ is the shear rate of slip system α. When a single relaxation process is considered, $\dot{\gamma}^\alpha$ is defined using an Eyring flow rule[11]:

$$\dot{\gamma}^\alpha = \dot{\gamma}_0^\alpha \underbrace{\exp\left(-\frac{\Delta U^\alpha}{RT}\right)}_{a} \underbrace{\sinh\left(\frac{\tau^\alpha}{\tau_0^c}\right)}_{b} \underbrace{\exp\left(\frac{\mu^\alpha \sigma_n^\alpha}{\tau_0^c}\right)}_{c}, \tag{23}$$

where $\dot{\gamma}_0^\alpha$ is the reference shear rate, τ_0^α is the reference shear strength, τ^α is the resolved shear stress. Part (a) of equation (23) describes the temperature dependence of the slip kinetics where, ΔU^α is the activation energy of each slip system, R is the universal gas constant and T is the absolute temperature. The stress dependence of the plastic flow is captured in part (b) of the equation. Finally, part (c) captures the effect of the normal stress of each slip plane (σ_n^α) on the plastic flow, where the parameter μ^α is the coefficient of normal stress dependency. Experimental results of tensile yield kinetics for initially isotropic Polyethylene at different temperatures and strain rates show that two relaxation processes contribute to the viscoplastic flow behaviour[11]. Based on these observations, two different flow processes are distinguished, as shown in Figure 3.

Figure 3.

The extended slip rate considering both processes I and II is given by[11]:

$$\dot{\gamma}^\alpha = \left[\frac{\dot{\gamma}_0^{c,\mathrm{I}} \exp\left(-\frac{\Delta U^{c,\mathrm{I}}}{RT}\right) \sinh\left(\frac{\tau}{\tau_0^{c,\mathrm{I}}}\right) \dot{\gamma}_0^{*,c,\mathrm{I+II}} \sinh\left(\frac{\tau}{\tau_0^{c,\mathrm{I+II}}}\right)}{\dot{\gamma}_0^{c,\mathrm{I}} \exp\left(-\frac{\Delta U^{c,\mathrm{I}}}{RT}\right) \sinh\left(\frac{\tau}{\tau_0^{c,\mathrm{I}}}\right) + \dot{\gamma}_0^{*,c,\mathrm{I+II}} \sinh\left(\frac{\tau}{\tau_0^{c,\mathrm{I+II}}}\right)}\right] \exp\left(\frac{\mu \sigma_n}{\tau_0^c}\right), \tag{24}$$

where $\tau_0^{\mathrm{I+II}}$ represents the shear stress dependence when both processes I and II are activated:

$$\tau_0^{c,\mathrm{I+II}} = \tau_0^{c,\mathrm{I}} + \tau_0^{c,\mathrm{II}}. \tag{25}$$

Also, the temperature dependent pre-exponential initial shear rate, $\dot{\gamma}_0^{*\ \mathrm{I+II}}$, includes contributions of two processes:

$$\dot{\gamma}_0^{*,c,\mathrm{I+II}} = 2\exp\left(-\frac{\tau_0^{c,\mathrm{I}}\ln\left[\frac{2}{\dot{\gamma}_0^{c,\mathrm{I}}}\exp\left(\frac{\Delta U^{c,\mathrm{I}}}{RT}\right)\right] + \tau_0^{c,\mathrm{II}}\ln\left[\frac{2}{\dot{\gamma}_0^{c,\mathrm{II}}}\exp\left(\frac{\Delta U^{c,\mathrm{II}}}{RT}\right)\right]}{\tau_0^{c,\mathrm{I}} + \tau_0^{c,\mathrm{II}}}\right). \tag{26}$$

It should be noted that super script $(^{\alpha})$ which refers to each slip system is omitted in relations (24)-(26) to avoid confusions.

Amorphous phase constitutive model

In this section, the initial *isotropic* model for the amorphous phase is described. The model is developed based on the EGP (Eindhoven Glassy Polymer) model[12,13] for amorphous polymers. A single mode model with two relaxation processes (α and β which will be referred to I and II, respectively) is adopted. The mechanical analogue of the single mode EGP model is shown in Figure 4.

Figure 4.

The total Cauchy stress is additively composed of the driving stress ($\boldsymbol{\sigma}_s^a$) and the hardening stress ($\boldsymbol{\sigma}_r^a$):

$$\boldsymbol{\sigma}^a = \boldsymbol{\sigma}_s^a + \boldsymbol{\sigma}_r^a. \tag{27}$$

The driving stress is dependent on the elastic deformation gradient and is composed of hydrostatic and deviatoric contributions indicated by superscript h and d, respectively, given by:

$$\boldsymbol{\sigma}_s^{ah} = -p^a\mathbf{I}; \qquad p^a = -K^a(J_e^a - 1), \tag{28}$$

$$\boldsymbol{\sigma}_s^{ad} = G^a\tilde{\mathbf{B}}_e^{ad}, \tag{29}$$

where K^a is the bulk modulus, G^a is the shear modulus. The isochoric elastic left Cauchy-Green deformation tensor is defined by:

$$\tilde{\mathbf{B}}_e^a = J_e^{a-\frac{2}{3}}\mathbf{F}_e^a \cdot \mathbf{F}_e^{aT}. \tag{30}$$

The hardening stress is dependent on the total isochoric deformation gradient:

$$\boldsymbol{\sigma}_r^a = G_r \tilde{\mathbf{B}}^{ad} \tag{31}$$

where G_r is the hardening modulus. A constitutive relation for the plastic deformation rate tensor is introduced in order to fully describe the deformation behaviour of the amorphous phase. The plastic deformation rate tensor is defined by:

$$\widetilde{\mathbf{D}}_p^a = \mathrm{sym}\left(\mathbf{F}_e \cdot \mathbf{L}_p \cdot \mathbf{F}_e{}^{-1}\right). \tag{32}$$

In this model, the plastic stretching tensor is given by:

$$\widetilde{\mathbf{D}}_p^a = \frac{\boldsymbol{\sigma}_s^{ad}}{2\eta}, \tag{33}$$

where η is the viscosity of the amorphous phase given by:

$$\eta = \frac{\tau}{\dot{\gamma}_p^a}, \tag{34}$$

and τ is the effective stress given by:

$$\tau = \sqrt{\frac{1}{2}\boldsymbol{\sigma}_s^{ad} : \boldsymbol{\sigma}_s^{ad}}. \tag{35}$$

In Equation (34), $\dot{\gamma}_p^a$ is the plastic shear rate which for two relaxation processes is given by:

$$\dot{\gamma}_p^a = \left(\frac{\dot{\gamma}_0^{a,\mathrm{I}} \sinh\left(\frac{\tau}{\tau_0^{a,\mathrm{I}}}\right) \dot{\gamma}_0^{a,\mathrm{I+II}} \sinh\left(\frac{\tau}{\tau_0^{a,\mathrm{I+II}}}\right)}{\dot{\gamma}_0^{a,\mathrm{I}} \sinh\left(\frac{\tau}{\tau_0^{a,\mathrm{I}}}\right) + \dot{\gamma}_0^{a,\mathrm{I+II}} \sinh\left(\frac{\tau}{\tau_0^{a,\mathrm{I+II}}}\right)}\right) \exp\left(-\frac{\mu\, p^a}{\tau_0^{a,\mathrm{II}}}\right), \tag{36}$$

where,

$$\dot{\gamma}_0^{a,\mathrm{I+II}} = 2\exp\left(-\frac{\tau_0^{a,\mathrm{I}} \ln(\frac{2}{\dot{\gamma}_0^{a,\mathrm{I}}}) + \tau_0^{a,\mathrm{II}} \ln(\frac{2}{\dot{\gamma}_0^{a,\mathrm{II}}})}{\tau_0^{a,\mathrm{I+II}}}\right), \tag{37}$$

$$\tau_0^{a,\mathrm{I+II}} = \tau_0^{a,\mathrm{I}} + \tau_0^{a,\mathrm{II}}. \tag{38}$$

The superscripts I and II denote two relaxation processes, τ is the effective stress, μ is the pressure dependency coefficient and τ_0^a is the shear strength of the amorphous phase. In Equation (36), p^a is the hydrostatic pressure of the amorphous phase. Kanters et al.[14] compared this approach with one that involves separate kinematics for the two relaxation processes and found that there is only a small difference between the aforementioned approaches.

Initial results

The mechanical behaviour of oriented tape is first predicted with the micro-mechanical model described in the previous section using an *isotropic* elasto-viscoplastic constitutive model for the amorphous phase. Based on wide angle X-ray scattering measurements, the initial orientation distribution was generated. The pole figures of the crystallographic and morphological orientations were generated to be consistent with the experimentally obtained pole figures[1]. As a quantitative measure for the orientation, the Hermans orientation factor was used[20]:

$$f_H = \frac{3 < \cos^2 \Phi > -1}{2}, \tag{39}$$

where Φ represents the angle between the crystallographic axis and a reference axis. The Hermans orientation factor varies between -0.5 and 1, where $f_H = -0.5$ represents an orthogonal orientation, $f_H = 0$ is obtained for a random orientation and $f_H = 1$ indicates a perfectly uniaxial orientation. Hermans factors are used to check if the generated samples properly represent the material. Figure 5 depicts pole figures of the crystallographic and lamellar orientations of oriented polyethylene tape with a draw ratio factor of 4 ($\lambda = 4$).

Figure 5.

Table 1 reveals that the Hermans factors of the created samples are close to the experimental ones. In[1], the volume fraction of the crystalline phase was estimated to be 60%.

Table 1: Hermans orientation factors for crystallographic orientations, obtained experimentally and from the generated samples.

	f_a	f_b	f_c
Experiment	-0.40	-0.29	0.70
Simulation	-0.37	-0.34	0.71

Before starting the simulations, the material properties of the crystalline lamellae and the amorphous domain are first presented.

Crystalline phase properties

The crystalline domains of PE possess an orthorhombic structure. Table 2 gives the lattice

parameters of the crystalline lamellae[29,30].

Table 2: Lattice parameters of PE crystals, all in $\mathring{A}$[29,30].

a	b	c
7.39	4.95	2.54

The elastic properties of the crystalline phase were obtained from Tashiro et al.[31] and are given in Table 3. The yield kinetics of the slip systems were determined such that the exper-

Table 3: Elastic properties of the crystalline lamellae of Polyethylene, all in GPa[31].

C_{11}	C_{22}	C_{33}	C_{12}	C_{13}	C_{23}	C_{44}	C_{55}	C_{66}
7.99	9.92	315.92	3.28	1.13	2.14	3.62	1.62	3.19

imentally obtained response of both the oriented and the original isotropic material[11] could be described for a range of strain rates. Here, the slip kinetics of the various slip systems were chosen to be parallel. Table 4 gives the values of slip kinetics used in this study.

Table 4: Slip kinetics of the crystalline lamellae of oriented PE[11].

	Process I			Process II		
Slip system	$\dot{\gamma}^{*,c,\mathrm{I}}_{0,T_{ref}}$ [s^{-1}]	$\Delta U^{c,\mathrm{I}}$ [kJ/mol]	$\tau_0^{c,\mathrm{I}}$ [MPa]	$\dot{\gamma}^{*,c,\mathrm{II}}_{0,T_{ref}}$ [s^{-1}]	$\Delta U^{c,\mathrm{II}}$ [kJ/mol]	$\tau_0^{c,\mathrm{II}}$ [MPa]
(100)[001]	6.5×10^{-20}	560	0.06	2.2×10^{-3}	110	0.7
(010)[001]	1×10^{-27}	1293	0.06	2.2×10^{-3}	110	0.7
{110}[001]	1×10^{-27}	1293	0.06	2.2×10^{-3}	110	0.7
(100)[010]	5×10^{-26}	867	0.06	2.2×10^{-3}	110	0.7
(010)[100]	1×10^{-27}	1293	0.06	2.2×10^{-3}	110	0.7
{110}[1$\bar{1}$0]	1×10^{-27}	1293	0.06	2.2×10^{-3}	110	0.7

Amorphous phase properties

The isotropic elastic material properties of the amorphous phase are defined as $G^a = 65$ MPa and $K^a = 3000$ MPa[11]. The viscoplastic (Eyring) properties for the amorphous domain are given in Table 7[11]. Figure 6 shows the total (sum of α and β relaxation processes) yield

Table 5: Viscoplastic properties of the amorphous domain of PE.

Process I			Process II		
$\dot{\gamma}_{0,T}^{a,\mathrm{I}}$ [s^{-1}]	$\Delta U^{a,\mathrm{I}}$ [kJ/mol]	$\tau_0^{a,\mathrm{I}}$ [MPa]	$\dot{\gamma}_{0,T}^{a,\mathrm{II}}$ [s^{-1}]	$\Delta U^{a,\mathrm{II}}$ [kJ/mol]	$\tau_0^{a,\mathrm{II}}$ [MPa]
2.1×10^{-39}	582	0.069	2.2×10^{-6}	110	0.805

kinetics of the slip systems and amorphous phase at room temperature.

Figure 6.

A comparison between the experimental results and model predictions obtained with the oriented crystallographic structure and an isotropic amorphous phase is given in Figure 7 for the three loading angles and three strain rates. All the model predictions in this study are converted from true stress-strain to engineering stress-strain curves in order to make a direct comparison to the experimental results.

Figure 7.

The discrepancy between the experimental results and simulations increases by increasing the strain rate and decreasing the loading angle. It should also be emphasized that in the simulations conducted in this study, the generated crystallographic orientation distribution well represents the crystallographic texture considering the WAXS measurements. However, as opposed to isotropic polymeric materials which have a higher compressive yield stress than their tensile yield stress, oriented polymers may show a considerably higher tensile yield strength in comparison to their compressive yield strength[33,34]. The yield behaviour and Bauschinger effect in injection molded Polyethylene at different loading angles and under different strain rates were studied by Senden et al.[34]. Senden et al.[35] modelled a strong Bauschinger effect in oriented Polycarbonate using an EGP based model including a viscous hardening branch. Consequently and considering the aforementioned observed Bauschinger effect in oriented Polyethylene, it was concluded that the amorphous phase orientation is not negligible and should be taken into account.

ANISOTROPIC MODEL FOR THE AMORPHOUS PHASE

There are different sources of anisotropy in oriented Polyethylene:

- Anisotropy associated to the crystalline lamellae:
  - Anisotropic elastic properties of each crystalline lamella;
  - Anisotropic viscoplastic properties of each crystalline lamella due to crystallographic slip processes;
- Anisotropy associated to the amorphous phase:
  - Anisotropic elasticity;
  - Internal stress due to the oriented elastic network;
  - Anisotropic viscoplastic flow;
- Difference in properties between oriented crystalline lamellae and amorphous domains.

In this study, an anisotropic model is developed for the amorphous phases in the micromechanical model. The three sources of anisotropy are incorporated in the model. In the following, each of these aspects is elaborated in detail.

Internal stress in the elastic network

Polymeric materials normally show a pressure dependent behaviour. For isotropic polymers, the yield stress in compression is slightly higher than under tensile conditions[33]. On the contrary, for oriented polymers, the yield stress in tensile loading may be considerably higher than in compression[33,34]. Senden et al.[34] studied the yield behaviour of injection moulded Polyethylene and showed a considerably higher yield strength in tension compared to compressive yield strength. Also, it was shown by Senden et al.[33,35] that by increasing the level of pre-stretch, the difference between tensile and compressive yield stress increases. The internal stress was found to be the main reason for the observed orientation dependent thermal shrinkage of PET films[15]. Furthermore, Poluektov et al.[15] showed that for oriented PET, it is necessary to include an internal stress into the elastic network of the amorphous phase in order to obtain a realistic macroscopic response for the creep compliance. Based on the aforementioned observations, an internal stress is incorporated into the elastic network for the amorphous phase of oriented Polyethylene. The internal stress, although different from

the classical kinematic hardening, will act as kinematic hardening. In order to include an internal pre-stress in the elastic elements (describing the molecular network) of the model, a pre-stretch deformation ($\mathbf{F}_d^a$) is applied to the hardening branch. Figure 8 depicts schematically how the pre-stretch deformation gradient is applied to the elastic network branch.

Figure 8.

The pre-stretch deformation gradient (i.e. affecting the initial state) in the elastic spring in the driving branch of the model is obtained by equilibrating the amorphous phase. Once the elastic pre-stretch in the driving branch is obtained, the initial plastic state is obtained so that the total deformation gradient of the driving branch is equal to identity (see Fig. 8). When the material is under deformation ($\mathbf{F}^a$), the deformation gradient tensor $\mathbf{F}_r^a$ of the hardening branch is obtained by:

$$\mathbf{F}_r^a = \mathbf{F}^a \cdot \mathbf{F}_d^a, \tag{40}$$

where, $\mathbf{F}^a$ is the deformation gradient of the amorphous phase and $\mathbf{F}_d^a$ is the imposed pre-stretching deformation gradient.

Anisotropic viscoplastic flow

As mentioned before, strong tension-compression asymmetry is observed in the deformation behaviour of oriented polymers[33,34]. Senden et al.[35] modelled the mechanical behaviour of Polycarbonate using an EGP based model including a viscous strain hardening contribution. Also, the cyclic uniaxial deformation of PC was modelled and a strong Bauschinger effect was properly captured. This indicates the presence of anisotropy in the visco-plastic flow. Besides, in preliminary simulations using the anisotropic constitutive model for the amorphous phase, combining with an internal stress, it was discovered that the viscoplastic flow rule should also be modified from isotropic to anisotropic so that the anisotropic rate dependence of the oriented material is also accurately modelled. The constitutive relation for the plastic deformation rate tensor is written as:

$$\widetilde{\mathbf{D}}_p^a = \dot{\gamma}_p^a \mathbf{N}, \tag{41}$$

where, $\dot{\gamma}^p$ is the plastic shear rate given by Equation (36). For the isotropic flow rule, the effective stress was given by Equation (35). In order to modify the flow rule of the model

to anisotropic flow, the equivalent stress (τ) is replaced with Hill's anisotropic effective stress[18,19] which is given by[34,36]:

$$\overline{\sigma}_H^2 = F\left(\sigma_{22}^* - \sigma_{33}^*\right)^2 + G\left(\sigma_{33}^* - \sigma_{11}^*\right)^2 + H\left(\sigma_{11}^* - \sigma_{22}^*\right)^2$$

$$+2L(\sigma_{23}^*)^2 + 2M(\sigma_{13}^*)^2 + 2N(\sigma_{12}^*)^2, \tag{42}$$

where $\boldsymbol{\sigma}^*$ is the driving stress tensor in the local coordinate system:

$$\boldsymbol{\sigma}^* = \mathbf{R}^a \cdot \boldsymbol{\sigma}_s^a \cdot \mathbf{R}^{aT}, \tag{43}$$

where, $\mathbf{R}^a$ is the rotation tensor. The anisotropy parameters in Equation (42) are defined by:

$$\begin{aligned} F &= \frac{1}{2}\left(\frac{1}{R_{22}^2} + \frac{1}{R_{33}^2} - \frac{1}{R_{11}^2}\right), \quad L = \frac{3}{2\ R_{23}^2}, \\ G &= \frac{1}{2}\left(\frac{1}{R_{11}^2} + \frac{1}{R_{33}^2} - \frac{1}{R_{22}^2}\right), \quad M = \frac{3}{2\ R_{13}^2}, \\ H &= \frac{1}{2}\left(\frac{1}{R_{11}^2} + \frac{1}{R_{22}^2} - \frac{1}{R_{33}^2}\right), \quad N = \frac{3}{2\ R_{12}^2}. \end{aligned} \tag{44}$$

The R_{ij} factors in relation (44) are the ratios between the corresponding anisotropic yield stress in ij direction to the reference yield stress. Introducing all R_{ij} parameters to unity reduces the anisotropic flow rule to the isotropic case with $\overline{\sigma}_H = \sqrt{3}\tau$. Accordingly, the plastic shear rate, given in Equation (36), is updated as:

$$\dot{\gamma}^p = \left(\frac{\dot{\gamma}_0^{a,\mathrm{I}} \sinh\left(\frac{\overline{\sigma}_H}{\sqrt{3}\tau_0^{a,\mathrm{I}}}\right) \dot{\gamma}_0^{a,\mathrm{I+II}} \sinh\left(\frac{\overline{\sigma}_H}{\sqrt{3}\tau_0^{a,\mathrm{I+II}}}\right)}{\dot{\gamma}_0^{a,\mathrm{I}} \sinh\left(\frac{\overline{\sigma}_H}{\sqrt{3}\tau_0^{a,\mathrm{I}}}\right) + \dot{\gamma}_0^{a,\mathrm{I+II}} \sinh\left(\frac{\overline{\sigma}_H}{\sqrt{3}\tau_0^{a,\mathrm{I+II}}}\right)}\right) \exp\left(-\frac{\mu\ p^a}{\tau_0^{a,\mathrm{II}}}\right). \tag{45}$$

In equation (41), $\mathbf{N}$ indicates the tensorial direction of flow and is given by:

$$\mathbf{N} = \mathbf{R}^{aT} \cdot \mathbf{N}^* \cdot \mathbf{R}^a, \tag{46}$$

where, $\mathbf{N}^*$ is given by:

$$\mathbf{N}^* = \frac{1}{\sqrt{3}} \frac{\partial \overline{\sigma}_H}{\partial \boldsymbol{\sigma}^*}. \tag{47}$$

The components of this tensor, $\mathbf{N}^*$, are obtained as:

$$N_{11}^* = \frac{1}{\overline{\sigma}_H}\left(\sigma_{11}^*\left(G + H\right) - \left(G\sigma_{33}^* + H\sigma_{22}^*\right)\right),$$

$$
\begin{aligned}
N_{22}^{*} &= \frac{1}{\overline{\sigma}_H}\left(\sigma_{22}^{*}\left(F+H\right)-\left(F\sigma_{33}^{*}+H\sigma_{11}^{*}\right)\right), \\
N_{33}^{*} &= \frac{1}{\overline{\sigma}_H}\left(\sigma_{33}^{*}\left(F+G\right)-\left(F\sigma_{22}^{*}+G\sigma_{11}^{*}\right)\right), \\
N_{12}^{*} &= \frac{2}{\overline{\sigma}_H}\left(N\sigma_{12}^{*}\right),\ N_{13}^{*} = \frac{2}{\overline{\sigma}_H}\left(M\sigma_{13}^{*}\right), \\
N_{23}^{*} &= \frac{2}{\overline{\sigma}_H}\left(L\sigma_{23}^{*}\right).
\end{aligned}
\tag{48}
$$

Anisotropic elasticity

Due to drawing, the polymer chains in the amorphous phase become preferentially oriented in the draw direction of the tape and as a result, a higher stiffness of the amorphous phase in the draw direction of the tape can be expected. Hence, the elastic isotropic behaviour of the amorphous phase needs to be modified to the anisotropic case as well.
The elastic stress-strain relation in the amorphous phase is given by:

$$
\mathbf{S}_s^a = {}^4\mathsf{C}^a : \mathbf{E}_e^a, \tag{49}
$$

where $\mathbf{S}_s^a$ is the elastic second Piola-Kirchhoff stress in the driving branch. The driving Cauchy stress is then given by:

$$
\boldsymbol{\sigma}_s^a = \frac{1}{J_e^a}\mathbf{F}_e^a \cdot \mathbf{S}_s^a \cdot \mathbf{F}_e^{aT}, \tag{50}
$$

with $\mathbf{F}_e^a$ the elastic deformation gradient tensor in the amorphous phase. In equation (49), the elastic Green-Lagrange strain, $\mathbf{E}_e^a$, is defined by:

$$
\mathbf{E}_e^a = \frac{1}{2}\left(\mathbf{F}_e^{aT} \cdot \mathbf{F}_e^a - \mathbf{I}\right), \tag{51}
$$

where, $\mathbf{I}$ is the second order identity tensor. In equation (49), ${}^4\mathsf{C}^a$ denotes the stiffness tensor of the amorphous phase which in matrix form, using the Voigt notation, has a similar matrix representation as the stiffness of the crystalline lamellae (Equation (20)). For an orthotropic

material, the compliance matrix, which is the inverse of the stiffness matrix, is given by:

$$\underline{\mathsf{S}}^a = \begin{bmatrix} \frac{1}{E_{11}} & -\frac{\nu_{21}}{E_{22}} & -\frac{\nu_{31}}{E_{33}} & 0 & 0 & 0 \\ -\frac{\nu_{12}}{E_{11}} & \frac{1}{E_{22}} & -\frac{\nu_{32}}{E_{33}} & 0 & 0 & 0 \\ -\frac{\nu_{13}}{E_{11}} & -\frac{\nu_{23}}{E_{22}} & \frac{1}{E_{33}} & 0 & 0 & 0 \\ 0 & 0 & 0 & \frac{1}{G_{12}} & 0 & 0 \\ 0 & 0 & 0 & 0 & \frac{1}{G_{13}} & 0 \\ 0 & 0 & 0 & 0 & 0 & \frac{1}{G_{23}} \end{bmatrix}, \tag{52}$$

where E_{ij} are the elastic moduli in different directions, ν_{ij} are the Poisson's ratios, G_{ij} are the shear moduli and the axes 1,2 and 3 correspond with the orthotropy axes.

RESULTS AND DISCUSSION

In this section, the material properties for the crystalline and amorphous phases of oriented PE are determined. Simulations are conducted using the the extended micro-mechanical model (including the anisotropic model for the amorphous phase) and the results are confronted with experimentally obtained stress-strain curves. Significant improvements in the model predictions are obtained and the comparisons with experimental results show the quantitative impact of the amorphous phase anisotropy.

Material properties

In this section, the material properties including the elastic properties and yield kinetics of the amorphous phase are determined. The lattice parameters, elastic properties and the yield kinetics of the crystalline lamellae, were given in the Section (see Tables 2, 3 and 4).

Amorphous phase properties

In order to recover the elastic properties for the amorphous phase, the isotropic case will be perturbed starting from the Young's modulus and Poisson's ratio, extended from the shear modulus and bulk modulus of the amorphous phase in isotropic PE (G^a = 65 MPa and K^a = 3000 MPa[11]). The Young's modulus in the draw direction of the tape is gradually increased in order to take into account the effect of drawing on the stiffness of the amorphous

phase in the draw direction. It was assumed that the main effect of the drawing process on the stiffness of the amorphous phase appears in the actual draw direction and thus the other two stiffness properties (E_{11}, E_{22}) are considered almost equal to the stiffness of the un-oriented amorphous phase (in isotropic PE). The results and comparison to experiments showed the assumption (regarding effects of drawing on the stiffness) to be reasonable. The Poisson's ratios are determined to best capture the experimental results and taking into account the symmetry of the compliance matrix. The shear moduli are also assumed to be the same as the shear modulus of isotropic PE. The elastic material properties of the amorphous phase are given in Table 6 and the viscoplastic (Eyring) properties for the amorphous domain are given in Table 7. The yield kinetics of the amorphous phase can have a large effect on

Table 6: Anisotropic elastic properties of the amorphous phase of oriented PE.

E_{11}, E_{22} (MPa)	E_{33} (MPa)	ν_{13}, ν_{23}	ν_{31}, ν_{32}	ν_{12}, ν_{21},	G_{12}, G_{13}, G_{23} (MPa)
200	600	0.1	0.3	0.3	65

Table 7: Viscoplastic properties of the amorphous domain of oriented PE.

Process I			Process II		
$\dot{\gamma}_{0,T}^{a,\mathrm{I}}$ [s^{-1}]	$\Delta U^{a,\mathrm{I}}$ [kJ/mol]	$\tau_0^{a,\mathrm{I}}$ [MPa]	$\dot{\gamma}_{0,T}^{a,\mathrm{II}}$ [s^{-1}]	$\Delta U^{a,\mathrm{II}}$ [kJ/mol]	$\tau_0^{a,\mathrm{II}}$ [MPa]
8.4×10^{-29}	582	0.32	7×10^{-4}	110	3.2

the rate sensitivity of the semi-crystalline polymer. The parameter τ_0 of the amorphous yield kinetics was increased to increase the rate dependency of the oriented amorphous phase and as a result, the rate dependency of the drawn PE. The various parameters of the oriented amorphous phase were determined in order to describe the entire stress-strain curve, including the post-yield response for all strain rates and loading angles. The yield kinetics of the amorphous phase and different slip systems of the crystalline lamellae at room temperature are shown in Figure 9.

Figure 9.

It should be emphasized that for determination of elastic and viscoplastic properties of the amorphous phase, the experimental results at strain rates of $\dot{\varepsilon} = 10^{-4}$ s^{-1} and $\dot{\varepsilon} = 10^{-3}$ s^{-1} are used.

Simulations and comparison to experiments

In order to understand the effect of the Hill parameters and the pre-stretch factor on the deformation behaviour of the oriented tape at different loading angles, parameter sensitivity analyses were performed and the effects of the mentioned parameters were investigated. According to the sensitivity analyses, the effect of the Hill parameters and also the pre-stretch factor on the deformation behaviour of the oriented tape (under each loading angle) was realized. Based on the physical meaning of the parameters and the observations in the parameter sensitivity analyses, the set of Hill parameters and pre-stretch factor, as given in Table 8, is adopted. As for the elastic and viscoplastic properties of the amorphous phase, the

Table 8: Hill anisotropy parameters and pre-stretch factor for the oriented tape ($\lambda = 4$).

Parameter	R_{11}	R_{22}	R_{33}	R_{12}	R_{13}	R_{23}	λ_0
Value	1	1	1.7	1	0.35	0.35	1.2

Hill parameters and pre-stretch factor are also identified based on the experimental results under strain rates of $\dot{\varepsilon} = 10^{-4}$ s^{-1} and $\dot{\varepsilon} = 10^{-3}$ s^{-1}. The identified properties are then used to capture the stress-strain curves at strain rate of $\dot{\varepsilon} = 10^{-2}$ s^{-1}. Simulations are conducted for the oriented tape on an aggregate of 200 inclusions. Figure 10 shows the simulation results along with the experimental stress-strain curves.

Figure 10.

Adequate agreements are obtained between the model predictions and experimental results. Although in some cases ($\dot{\varepsilon} = 10^{-2}$ s^{-1}, $\phi = 0°, 20°$), the model predictions do not match the experimental results perfectly, comparison with Figure 7 still shows a significant improvement of the model predictions. Also, the dominant role of the anisotropy of the amorphous phase is noticeable. It was observed that the initially strongly oriented crystallographic texture further orients with the chain direction towards the drawing axis during deformation. Figure 11 shows the value of the von Mises effective stress of the amorphous phase and the crystalline lamella of each composite inclusion at the end of the deformation, under a strain rate of $\dot{\varepsilon} = 10^{-2}$ s^{-1} at different loading angles. The values of the effective stress are shown in pole figures which depict the distributions of the lamellar normals.

Figure 11.

Clearly, by increasing the loading angle, the effective stress of both phases decreases. For loading angles of $\phi = 0°$ and $\phi = 20°$, the amorphous phase of the inclusions which are less aligned with the loading direction (higher angle between the lamellar normal and loading direction), have higher stresses. It is also seen that for $\phi = 20°$ and also $\phi = 0°$, the inclusions with large amorphous stresses are differently oriented than inclusions with large crystalline stresses. Figures 12 and 13 show the plastic shear rate of the chain slip and transverse slip systems at the yield point, normalized by the applied strain rate ($\dot{\varepsilon} = 10^{-2}$ s^{-1}), in pole figures that show the distributions of the lamellar normals for loading angles of $\phi = 0°$ and $\phi = 50°$, respectively.

Figure 12.

The transverse slip systems for the sample taken along the draw direction of the oriented tape ($\phi = 0°$), are less active compared to the chain slip systems. Also, it can be observed that for $\phi = 0°$ the slip system (100)[001] is the most dominant one.

Figure 13.

In contrast to a loading of $\phi = 0°$, the activity of the transverse slip systems is higher than the chain slip systems for a loading angle of $\phi = 50°$. It can also be seen that for $\phi = 50°$ one chain slip system, (010)[001], and one transverse slip system, (100)[010], are not active.

CONCLUSIONS

The objective of this study was to model and capture the anisotropic mechanical behaviour of oriented Polyethylene within a micro-mechanical approach. Drawn PE tapes show a highly anisotropic and highly rate-dependent behaviour. There are different sources of anisotropy in these materials. As discussed by Sedighiamiri et al.[1] and shown in Section , considering the anisotropic behaviour and oriented distribution of the crystalline lamellae does not suffice to accurately predict the mechanical behaviour of oriented PE tapes. Accordingly, in this study, an anisotropic model for the amorphous phase was incorporated in the micro-mechanical model. Anisotropic elasticity, internal stress into the elastic network and an anisotropic visco-plastic flow were included for this purpose. The modified model adequately predicts the experimental results and remarkable improvements were obtained compared to the original

(partially isotropic) model predictions. It can be concluded that the effect of the anisotropy of the amorphous phase in oriented PE tapes is significant and it can not be neglected.

ACKNOWLEDGMENTS

The authors gratefully acknowledge ExxonMobil corporation for financial support of this study.

References

1. A. Sedighiamiri, D.J.A. Senden, D. Tranchida, L.E. Govaert and J.A.W. van Dommelen, *Comp. Mater. Sci.* **2014**, 82, 415.

2. J.A.W. van Dommelen, D.M. Parks, M.C. Boyce, W.A.M. Brekelmans and F.P.T. Baaijens, *J. Mech. Phys. Solids* **2003**, 51(3), 519.

3. D.M. Parks and S. Ahzi, *J. Mech. Phys. Solids* **1990**, 38(5), 701.

4. B.J. Lee, D.M. Parks and S. Ahzi, *J. Mech. Phys. Solids* **1993**, 41, 1651.

5. B.J. Lee, A.S. Argon, D.M. Parks, S. Ahzi and Z. Bartczak, *Polymer* **1993**, 34, 3555.

6. B.J. Lee, S. Ahzi and R.J. Asaro, *Mech. Mater.* **1995**, 20(1), 1.

7. S. Ahzi, B.J. Lee and R.J. Asaro, *Mater. Sci. Eng. A* **1994**, 189(1-2), 35.

8. S. Nikolov and I. Doghri, *Polymer* **2000**, 41(5), 1883.

9. S. Nikolov, I. Doghri, O. Pierard, L. Zealouk and A. Goldberg, *J. Mech. Phys. Solids* **2002**, 50(11), 2275.

10. A. Sedighiamiri, L.E. Govaert and J.A.W. van Dommelen, *J. Polym. Sci. B* **2011**, 49(18), 1297.

11. A. Sedighiamiri, L.E. Govaert, M.J.W. Kanters and J.A.W. van Dommelen, *J. Polym. Sci. B* **2012**, 50(24), 1679.

12. L.E. Govaert, P.H.M. Timmermans and W.A.M. Brekelmans, *J. Eng. Mater. Tech.* **2000**, 122, 177.

13. L.C.A. van Breemen, E.T.J. Klompen, L.E. Govaert and H.E.H. Meijer, *J. Mech. Phys. Solids* **2011**, 59(10), 2191.

14. M.J.W. Kanters, K. Remerie, L.E. Govaert, *Poly. Eng. Sci.* **2016**, 56, 676.

15. M. Poluektov, J.A.W. van Dommelen, L.E. Govaert, and M.G.D. Geers, *Model. Simul. Mater. Sci. Eng* **2014**, 22(5), 055024.

16. M. Poluektov, J.A.W. van Dommelen, L.E. Govaert, I. Yakimets and M.G.D. Geers, *J. Mater. Sci.* **2013**, 48(10), 3769.

17. M. Poluektov, J.A.W. van Dommelen, L.E. Govaert, I. Yakimets and M.G.D. Geers, *Model. Simul. Mater. Sci. Eng* **2013**, 21(8), 085015

18. R. Hill, *Proc R Soc Lond* **1948**, 193, 281.

19. R. Hill, The mathematical theory of plasticity, Oxford University Press, **1950**, Chapter XII: plastic anisotropy.

20. P.H. Hermans, J.J. Hermans, D. Vermaas and A. Weidinger, *J. Mater. Sci.* **1948**, 3, 1.

21. G.I. Taylor, *J. Inst. Metals* **1938** 62, 307.

22. G. Sachs, *Zeitschrift des Vereines Deutscher Ingenieure* **1928**, 72, 734.

23. Bilby, A., Lardner, L.R.T., Stroh, A.N., Actes du IXe congrés international de mècanique appliquèe (Bruxelles, 1956) 8, 35.

24. A. Galeski, *Prog. Polym. Sci.* **2003**, 28, 1643.

25. L. Lin and A.S. Argon, *J. Mater. Sci.* **1998**, 29(2), 294.

26. P.B. Bowden and R.J. Young, *J. Mater. Sci.* **1974**, 9, 2034.

27. Z. Bartczak, R.E. Cohen and A.S. Argon, *Macromolecules* **1992**, 25, 4692.

28. Z. Bartczak, A.S. Argon and R.E. Cohen, *Macromolecules* **1992**, 25, 5036.

29. L.E. Govaert, B. Brown and P. Smith, *Macromolecules* **1992**, 25, 3480.

30. T.L. Phillips and S. Hanna, *Polymer* **2005**, 46, 11003.

31. K. Tashiro, M. Kobayashi and H. Tadakoro, *Macromolecules* **1978**, 11, 914-918.

32. J.A.W. van Dommelen, M. Poluektov, A. Sedighiamiri and L.E. Govaert, *Mech. Res. Commun.* **2016**, 80, 4.

33. D.J.A. Senden, J.A.W. van Dommelen and L.E. Govaert, *J. Polym. Sci. B* **2010**, 48 (13), 1483.

34. D.J.A. Senden, G.W.M. Peters, L.E. Govaert and J.A.W. van Dommelen, *Polymer* **2013**, 54(21), 5899.

35. D.J.A. Senden, S. Krop, J.A.W. van Dommelen and L.E. Govaert, *J. Polym. Sci. B* **2012**, 50(24), 1680.

36. T.B. van Erp, C.T. Reynolds, T. Peijs, J.A.W. van Dommelen and L.E. Govaert, *J. Polym. Sci. B* **2009**, 47(20), 2026.

37. S. Gautam, S. Balijepalli and G.C. Rutledge, *Macromolecules* **2000**,33, 9136.

Figure 1: (a): Schematic representation of the samples cut from the oriented tape, (b): Experimental stress-strain curves for the oriented tape for different strain rates at room temperature.

Figure 2: (a): Composite inclusion consisting of a crystalline lamella and an amorphous layer; (b): Schematic representation of an aggregate of randomly distributed composite inclusions.

Figure 3: Schematic representation of two relaxation processes contributing to the yield kinetics.

Figure 4: Mechanical analogue of the single mode EGP model.

Figure 5: Equal area pole figures of the lamellar and crystallographic orientation distributions for pre-stretched PE tape with draw ratio of 4.

Figure 6: Total slip kinetics of the crystalline lamellae and the yield kinetics of the amorphous phase (sum of α and β processes) at room temperature adopted in the initial simulations.

Figure 7: Experimental results and predicted stress-strain curves with the original model for the oriented PE tape under different loading angles and at different strain rates

Figure 8: Schematic representation of application of pre-stretch in the amorphous model.

Figure 9: Total yield kinetics of the amorphous phase and crystalline lamellae of the oriented tape.

Figure 10: Experimental results and predicted stress-strain curves with the fully anisotropic model for the oriented tape under different loading angles and different strain rates

Figure 11: Equivalent stress of the amorphous and crystalline phases of the oriented tape at the end of the deformation under a strain rate of $\dot{\varepsilon} = 10^{-2}$ s^{-1}, shown in pole figures that show the distributions of the lamellar normals, at different loading angles, (a): $\phi = 0°$, amorphous phase, (b): $\phi = 0°$, crystalline phase, (c): $\phi = 20°$, amorphous phase, (d): $\phi = 20°$, crystalline phase, (e): $\phi = 50°$, amorphous phase, (f): $\phi = 50°$, crystalline phase.

Figure 12: The normalized plastic slip rates of the chain and transverse slip systems of the oriented tape at the yield point and under a strain rate of $\dot{\varepsilon} = 10^{-2}$ s^{-1}, at loading angle $\phi = 0°$ depicted in pole figures which represent the distributions of the lamellar normals.

Figure 13: The normalized plastic slip rates of the chain and transverse slip systems of the oriented tape at the yield point and under a strain rate of $\dot{\varepsilon} = 10^{-2}$ s^{-1}, at loading angle $\phi = 50°$ shown in pole figures which depict the distributions of the lamellar normals.

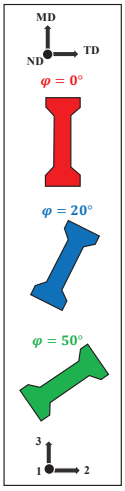

(a)

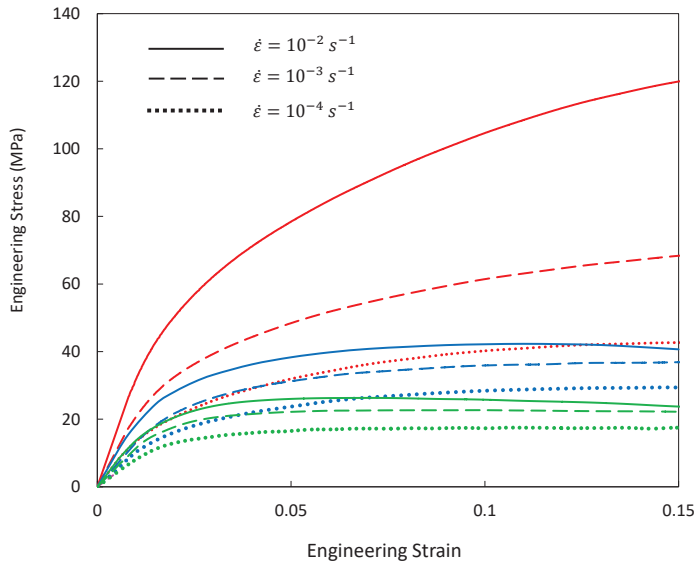

(b)

Figure 1.

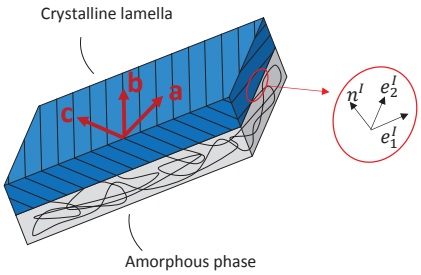

(a)

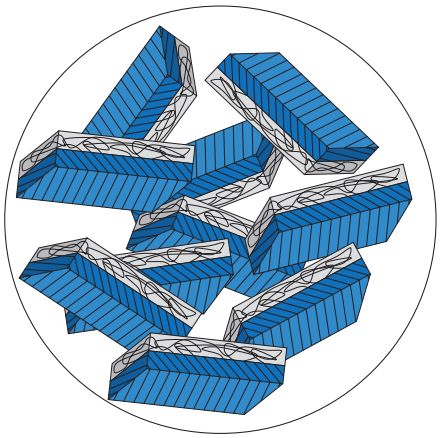

(b)

Figure 2.

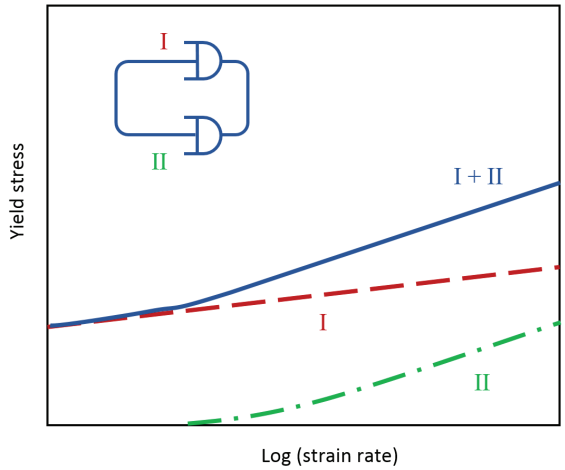

Figure 3.

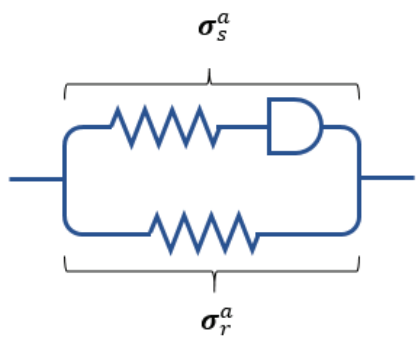

Figure 4.

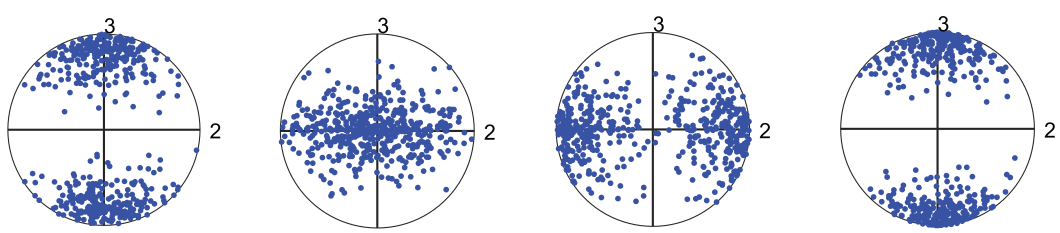

normals (100) (010) (001)

Figure 5.

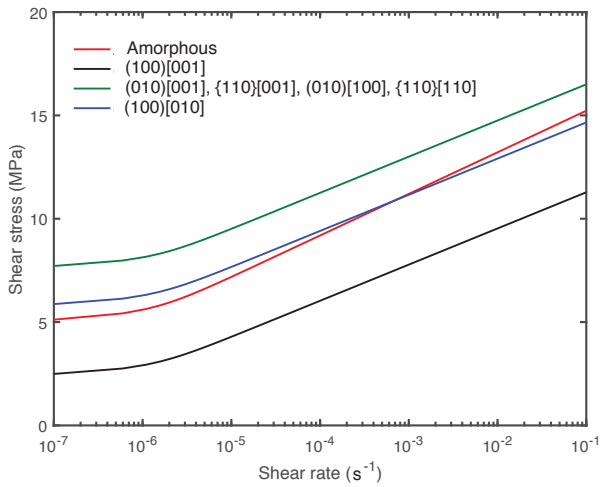

Figure 6.

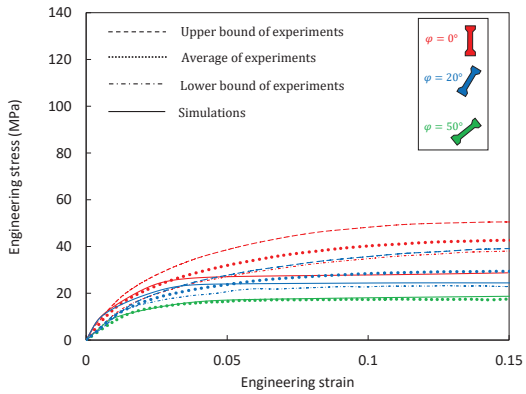

(a): $\dot{\varepsilon} = 10^{-4}$ s^{-1}

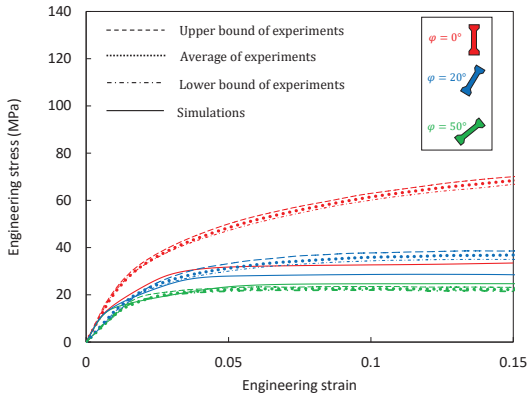

(b): $\dot{\varepsilon} = 10^{-3}$ s^{-1}

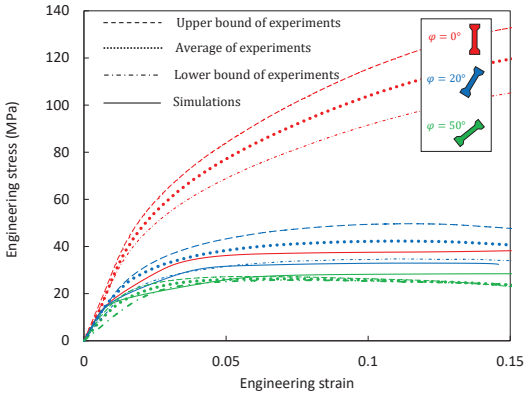

(c): $\dot{\varepsilon} = 10^{-2}$ s^{-1}

Figure 7.

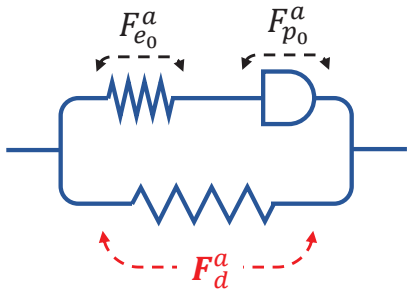

Figure 8.

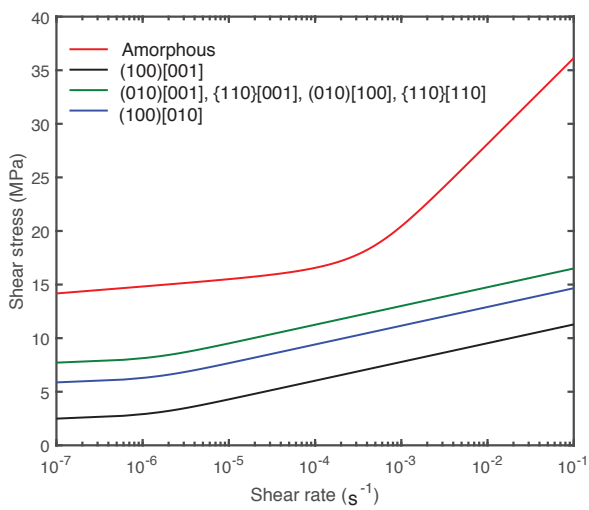

Figure 9.

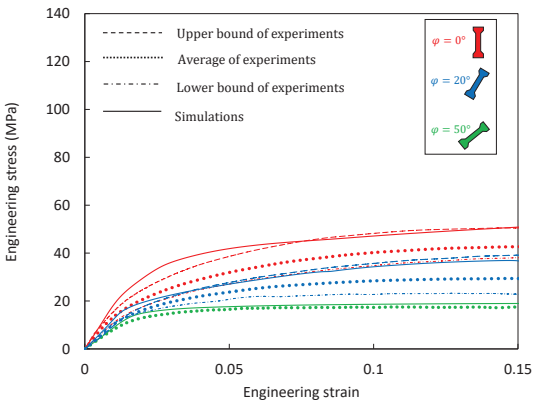

(a): $\dot{\varepsilon} = 10^{-4}$ s^{-1}

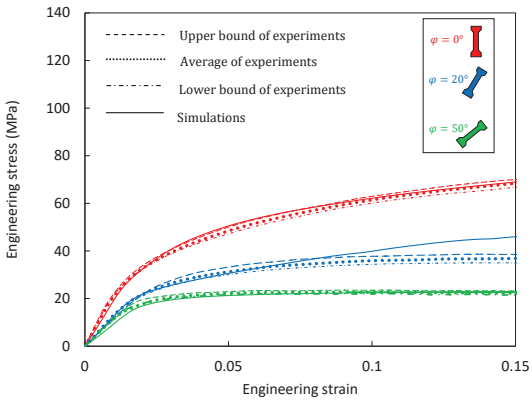

(b): $\dot{\varepsilon} = 10^{-3}$ s^{-1}

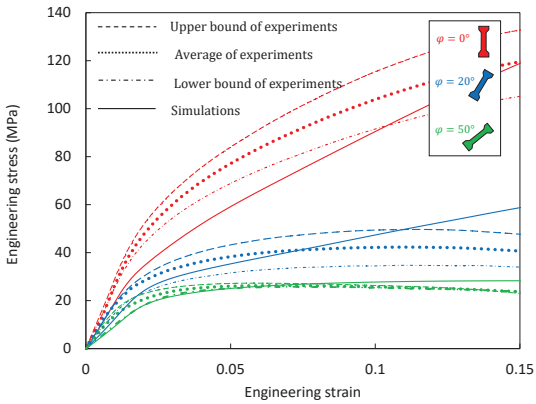

(c): $\dot{\varepsilon} = 10^{-2}$ s^{-1}

Figure 10.

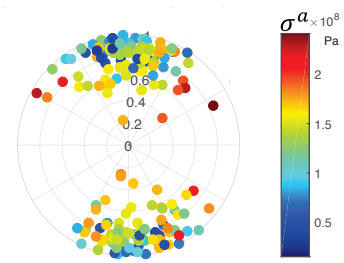

(a) 0°

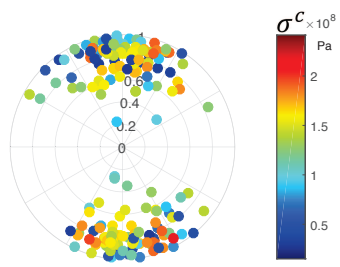

(b) 0°

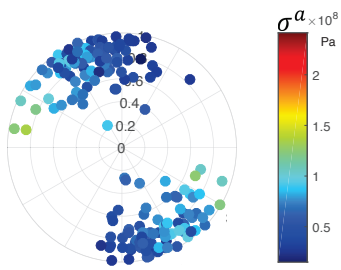

(c) 20°

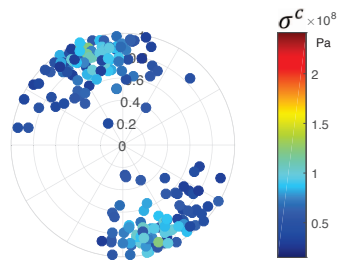

(d) 20°

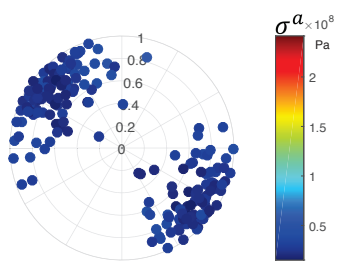

(e) 50°

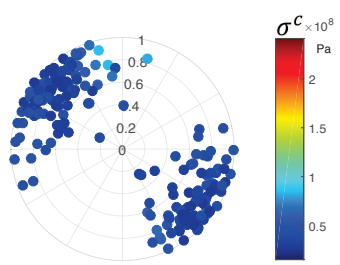

(f) 50°

Figure 11.

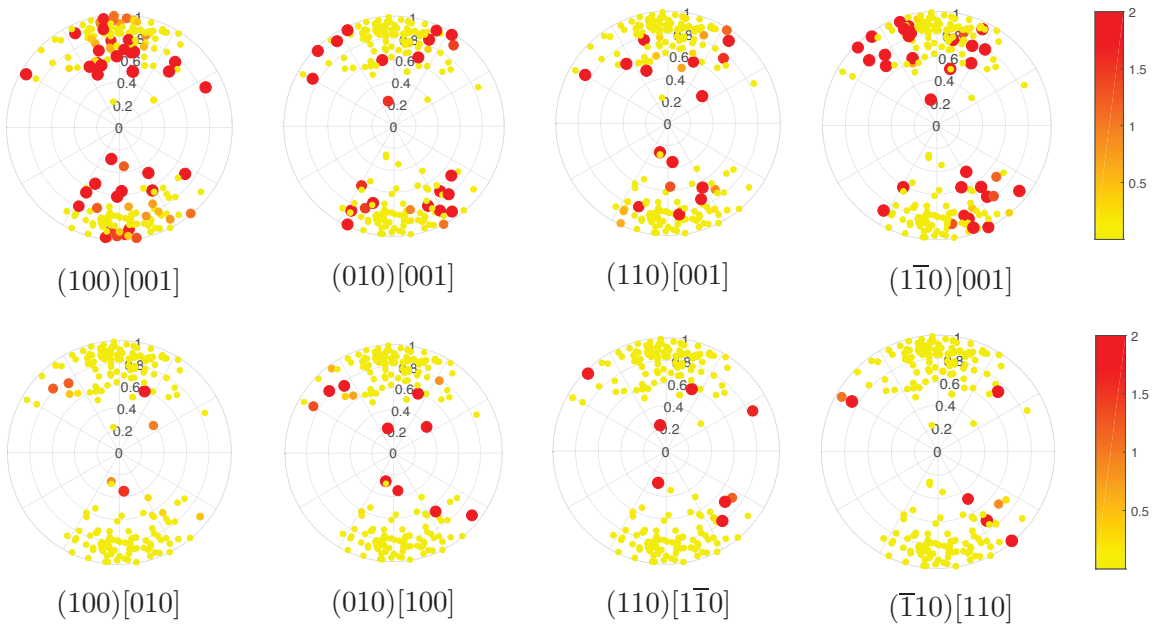

Figure 12.

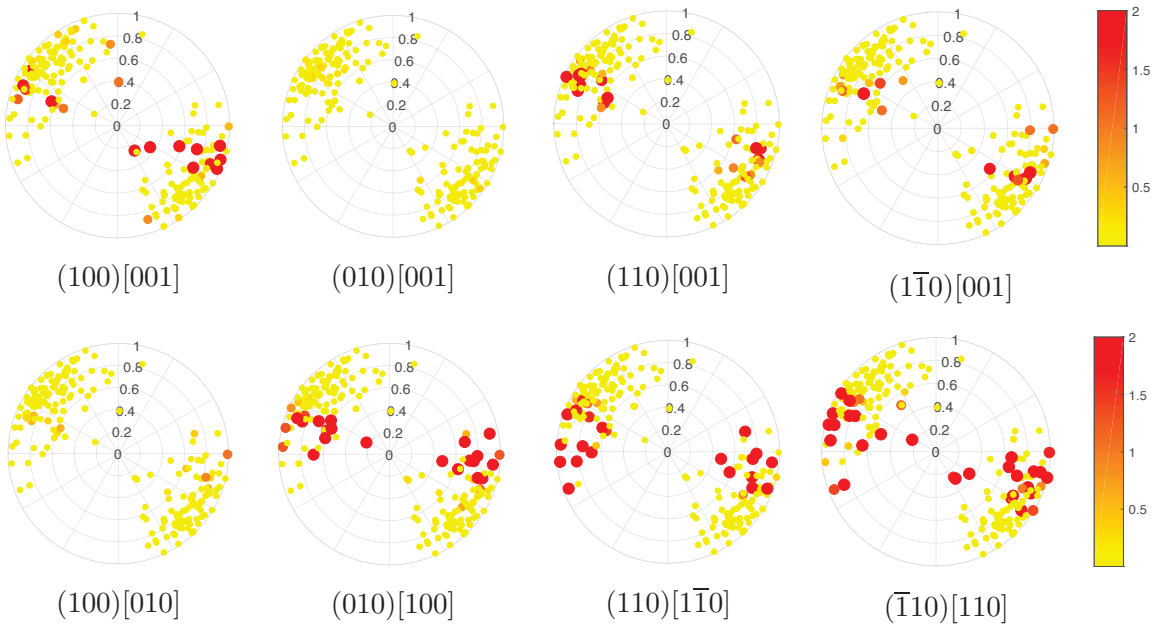

Figure 13.